Ultrahighly Saturated Structural Colors Enhanced by Multipolar-Modulated Metasurfaces

Bo Yang,[†] Wenwei Liu,[†] Zhancheng Li,[†] Hua Cheng,[†] Duk-Yong Choi,[*,‖,⊥] Shuqi Chen,[*,†,‡,§] and Jianguo Tian[†,‡]

[†]The Key Laboratory of Weak Light Nonlinear Photonics, Ministry of Education, School of Physics and TEDA Institute of Applied Physics and [‡]Renewable Energy Conversion and Storage Center, Nankai University, Tianjin 300071, China
[§]The collaborative Innovation Center of Extreme Optics, Shanxi University, Taiyuan, Shanxi 030006, China
[‖]Laser Physics Centre, Research School of Physics and Engineering, Australian National University, Canberra, ACT 2601, Australia
[⊥]College of Information Science and Technology, Jinan University, Guangzhou 510632, China

S *Supporting Information*

ABSTRACT: Colors with high saturation are of prime significance for display and imaging devices. So far, structural colors arising from all-dielectric metasurfaces, particularly amorphous silicon and titanium oxide, have exceeded the gamut of standard RGB (sRGB) space. However, the excitation of higher-order modes for dielectric materials hinders the further increase of saturation. Here, to address the challenge, we propose a new design strategy of multipolar-modulated metasurfaces with multi-dielectric stacked layers to realize the deep modulation of multipolar modes. Index matching between layers can suppress the multipolar modes at nonresonant wavelength, resulting in the dramatic enhancement in the monochromaticity of reflection spectra. Ultrahigh-saturation colors ranging from 70% to 90% with full hue have been theoretically and experimentally obtained. The huge gamut space can be realized in an unprecedented way, taking up 171% sRGB space, 127% Adobe RGB space, and 57% CIE space. More interestingly, the coverage for Recommendation 2020 (Rec. 2020) space, which almost has not been successfully realized so far, can reach 90%. We anticipate that the proposed multipolar-modulated metasurfaces are promising for the enlargement of the color range for high-end and advanced display applications.

KEYWORDS: *Multi-dielectric metasurface, structural colors, ultrahigh saturation, deep modulation, Adobe RGB space*
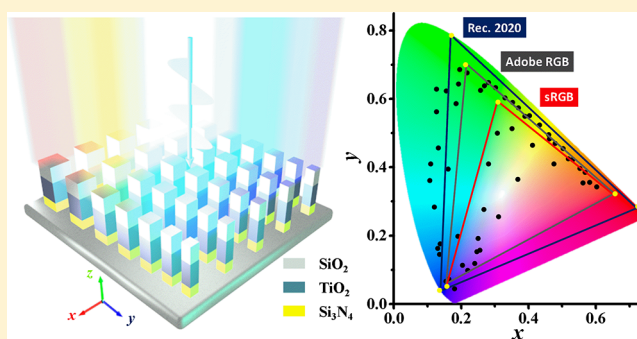
Colors, the important carrier of visual information in the nature, have been intensively studied since ancient times. Compared with conventional colors generated from chemical pigments by light absorption or light emission, structural colors by light scattering have attracted burgeoning interest due to high resolution, fine compactness, and superior durability in the past decades.[1−3] With the drastic development of micronanofabrication technologies, full-hue-modulation structural colors at the sub-wavelength scale have been extensively realized by plasmonic metasurfaces[4−11] and dielectric metasurfaces.[12−16] However, generating highly saturated structural colors, which are vital in displays and imaging, is still a huge challenge owing to the inherent ohmic loss for plasmonic nanostructures[13−15] or substrate effects for silicon nanostructures.[17,18] To achieve purer colors, several attempts have been made by designing the geometry of nanopixels skillfully.[19−25] Up to now, Dong et al. have remarkably demonstrated a largest color palette occupying about 120% of sRGB space by utilizing the coating layer of silicon nitride (Si_3N_4) to mimic amorphous silicon nanopillars in free space.[25] Although wide color gamut

surpassing sRGB space has been achieved, the saturation still needs to be further enhanced to meet more standard color spaces used in practice on the International Commission on Illumination (CIE) 1931 chromaticity diagram.[26] For instance, Adobe RGB color space with more saturated aquamarine blue is necessary for high-end camera and advanced imaging applications.[27]

Titanium dioxide (TiO_2), with a relatively high refractive index and negligible extinction coefficient, can be a good candidate to further increase the saturation at visible wavelengths. Because TiO_2 nanostructures can simultaneously support electric dipoles and magnetic dipoles in Mie resonance, TiO_2 metasurfaces have been successful used in high-quality visible metalens,[28,29] autofocusing airy beams,[30] chiral holograms,[31] and so on. In particular, highly saturated colors with wide gamuts have been realized via all-TiO_2
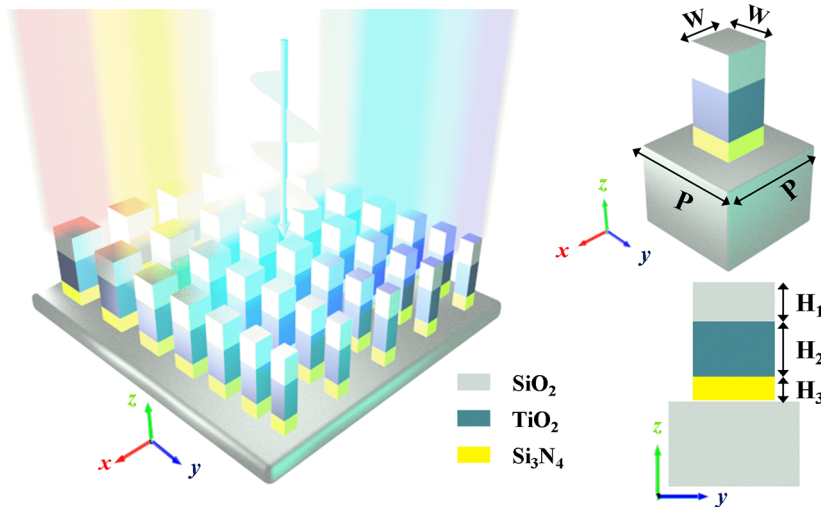
Figure 1. Structural design of the multi-dielectric metasurface under normally visible illumination. Each unit cell consists of a 100 nm thick (H_1) SiO_2 capping layer, a 140 nm thick (H_2) TiO_2 spacer layer, and a 60 nm thick (H_3) Si_3N_4 layer from top to bottom.
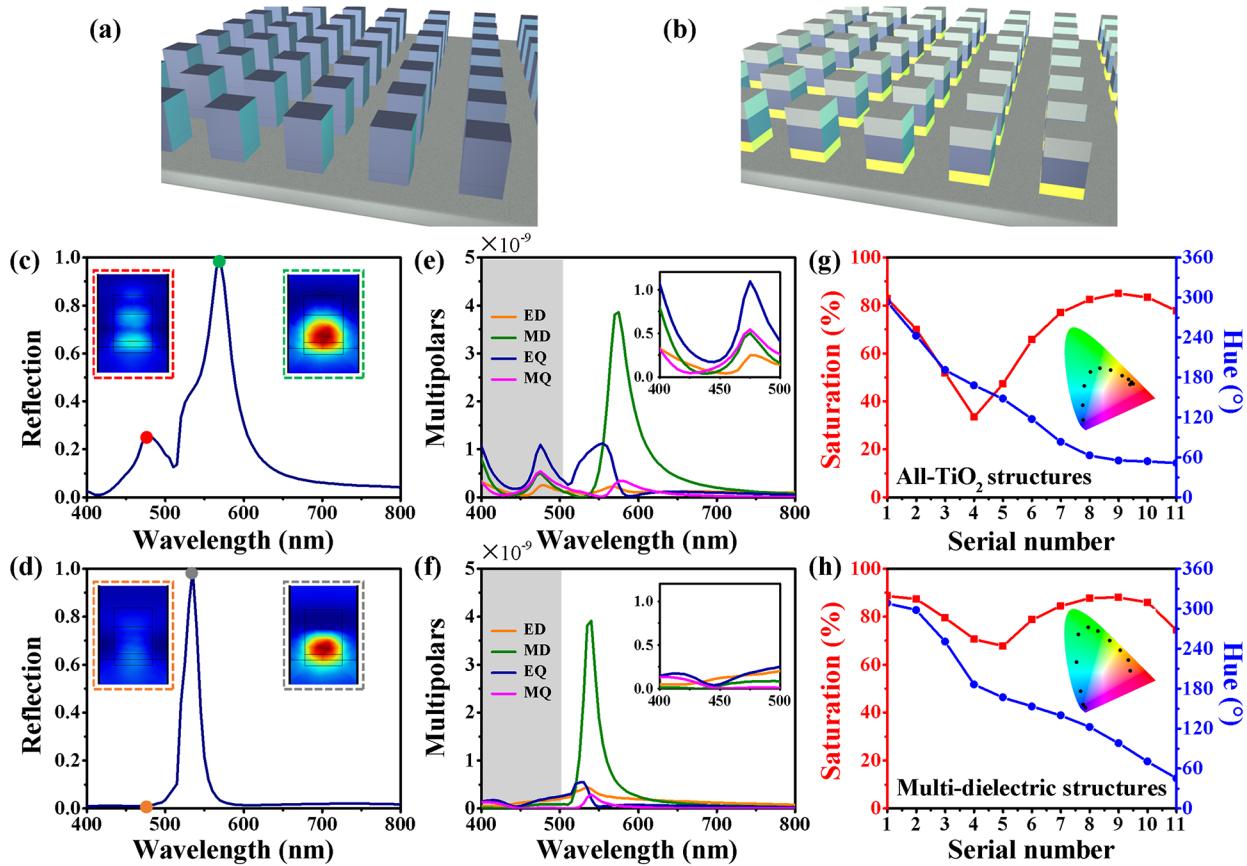
Figure 2. Optical characteristics and colors representation for (a) all-TiO_2 structures and (b) multi-dielectric structures. (c, d) Simulated reflection spectra of nanoblocks with a period of 350 nm and a width of 200 nm. The insets show the magnetic field distribution of all-TiO_2 structures at 480 nm (red dashed box)/570 nm (green dashed box) and multi-dielectric structures at 480 nm (orange dashed box)/ 535 nm (gray dashed box), respectively. (e, f) Multipolar decomposition of scattering cross-sections in terms of electric dipole (ED), magnetic dipole (MD), electric quadrupole (EQ), and magnetic quadrupole (MQ). The insets show the magnification of decomposition at wavelength ranging from 400 to 500 nm. (g, h) The simulated saturation and hue of corresponding reflected colors as functions of n. The serial number n increases from 1 to 11 with the period varying from 300 to 400 nm when the gap is fixed at 150 nm. The insets are the 1931 CIE diagram for all-TiO_2 and multi-dielectric structures, respectively.

nanostructures.[32,33] Nevertheless, owing to the excitation of high-order modes of TiO_2 nanostructures at shorter wavelengths,[32,34] the defective monochromaticity of reflection spectra severely hinders the further increasing of saturation. The saturation of structural colors, especially the aquamarine blue area, is still limited.

To address the challenge of highly saturated colors, a feasible strategy that can deeply modulate quadrupole modes of Mie resonance is greatly desired. Generally speaking, multiple resonances can realize full modulation of higher order modes by polymer metasurface arising from the interference between dipole resonant mode and subradiant mode.[35−38] Most recently, nearly 100% modulation depth of multiple Fano resonances has been reached at near-infrared wavelength.[36] However, the interaction between resonant modes is very complicated and can result in huge simulation work to accomplish suppression of quadrupole in visible regime. Polymer unit cells consisting of several nanostructures may also hinder integration on devices and modulation at deep sub-wavelengths.

Here, to dramatically enhance the saturation and gamut space of structural colors, we present a design strategy of deep modulation based on multi-dielectric metasurfaces with SiO_2, TiO_2, and Si_3N_4 from top to bottom at visible wavelengths. In contrast to the all-TiO_2 nanostructures, index matching of SiO_2 capping layer between the TiO_2 spacer layer and air, and Si_3N_4 bottom layer between silica substrate and TiO_2 layer at multi-dielectric nanostructures can enhance monochromaticity via suppressing excitation of multipolar modes, especially electric quadrupoles, at shorter wavelength. Based on the multi-dielectric design, we demonstrate highly saturated colors ranging from 70% to 90% theoretically and experimentally. The novel and unique nanostructures we designed can, against precedent, realize a huge gamut space taking up 171% sRGB space, 127% Adobe RGB space, and 57% CIE space. More interestingly, the coverage for Rec. 2020 space, which almost has not been successfully realized so far, can reach 90%. Furthermore, the quality of aquamarine blue color from 495 to 510 nm is significantly improved compared with the monodielectric nanostructures. Our proposed multi-dielectric nanostructures can be vastly used to enlarge the color information in high-end display and imaging applications.

Figure 1 illustrates the schematic of the multi-dielectric metasurface we proposed, which is composed of the array of stacked-layer nanoblocks on silica substrate. Each unit cell is made of a vertically stacked 100 nm thick (H_1) SiO_2 capping layer, a 140 nm thick (H_2) TiO_2 spacer layer, and a 60 nm (H_3) thick Si_3N_4 layer from top to bottom with varying periods (P) of square lattices and widths (W) of nanoblocks. The gap size (g) presents the distance between adjacent nanoblocks, namely, $g = P − W$. According to optical measurement, the refractive index of TiO_2 is about 2.41 at 500 nm, and the extinction coefficient can be negligible in the visible band. The higher order resonant modes at shorter wavelength can be deeply modulated by utilizing the index matching of SiO_2 capping layer between the TiO_2 layer and air and the Si_3N_4 layer between the silica substrate and TiO_2 layer.

To prove the role of the multi-dielectric design, we compare the performances of all-TiO_2 nanostructures with multi-dielectric nanostructures in Figure 2. As the sketches show in Figure 2a,b, 300 nm thick nanoblocks with width of 200 nm are arranged in a square lattice with period of 350 nm. Figure 2c,d present the simulated reflection spectra of all-TiO_2 and multi-dielectric nanostructures by finite-element-method commercial software (COMSOL Multiphysics),[39] respectively. For all-TiO_2 nanostructures, there is a minor peak at 480 nm, which seriously affects the monochromaticity of visible spectra. However, the reflection peak vanishes in multi-dielectric nanostructures. The insets of Figure 2c,d show the simulated

magnetic field distribution $|H|$ at different resonant wavelengths. At 480 nm, the all-TiO_2 nanostructure holds stronger excitation of magnetic field (indicated in red dashed box) at the minor reflection peak than that (indicated in orange dashed box) of the non-resonant multi-dielectric nanostructures. As for the dominating resonant wavelength (570 and 535 nm, respectively), the distributions of magnetic field for two kinds of nanostructures are both confined in the center of the nanoblocks. The suppression of magnetic field at the wavelength of 480 nm indicates that the multi-dielectric nanostructures can manipulate the excitation of Mie resonance. To further investigate the modulation depth of multi-dielectric design, we decompose the multipolar modes of scattering cross-sections into electric dipole (ED), magnetic dipole (MD), electric quadrupole (EQ), and magnetic quadrupole (MQ) modes, as shown in Figure 2e,f. In the case of harmonic excitation $\exp(i\omega t)$, the scattering cross-section can be expressed in terms of multipolar modes as:

$$I = \frac{2\omega^4}{2c^3}|\mathbf{P}|^2 + \frac{2\omega^4}{2c^3}|\mathbf{M}|^2 + \frac{\omega^6}{5c^5}Q_{\alpha\beta}Q_{\alpha\beta} + \frac{\omega^6}{20c^5}M_{\alpha\beta}M_{\alpha\beta}$$

(1)

where $\mathbf{P}$, $\mathbf{M}$, $Q_{\alpha\beta}$, and $M_{\alpha\beta}$ are ED, MD, EQ, and MQ moments, respectively (see the details in Figure S1).[40−42] In Figure 2e, the decomposition calculations show that the minor resonant peak is collectively excited by multipolar modes (especially EQ mode) in all-TiO_2 nanostructures. The multi-dielectric nanostructures, however, maximally eliminate the impact of multipolar excitation at short wavelength, as presented in Figure 2f.

In all-TiO_2 nanostructures, some resonant modes occur at the short wavelengths, leading to reductive saturation of the generated structural colors. These resonant modes can be attributed to the Fabry−Perot-like resonances between the boundaries of the all-TiO_2 nanostructures. To interpret the reasons and design strategy, we simulated two models with different setups of dielectric layers (see the details in Figure S2). First, we adopted gradient-index (GRIN) layers to realize the anti-reflection condition at the boundaries of air/TiO_2 and TiO_2/substrate. The refractive indices of the capping and bottom layers are set sinusoidally so that the indices vary smoothly. Second, we adopted index-matching conditions in the capping and bottom layers and optimized the reflection at 480 nm incidence. In both of the theoretical models, the multipolar modes at short working wavelengths are significantly suppressed, which directly demonstrates that the anti-reflection coating is vital for high saturation of dielectric structural colors. We selected SiO_2 and Si_3N_4 as the capping and bottom layers to realize the index matching condition and minimized the first peak of all-TiO_2 nanostructures at 480 nm. Although the refractive indices approximately satisfy $n_{SiO_2} \approx \sqrt{n_{TiO_2}n_{air}}$ and $n_{Si_3N_4} \approx \sqrt{n_{TiO_2}n_{silica}}$, there are still some deviations from the ideal refractive index dispersion because the sub-wavelength structure could also lead to the deviation of the effective index due to Mie scattering effect. The final optimized thicknesses of the SiO_2 and Si_3N_4 layers are 100 and 60 nm, respectively. The total height of the nanostructure is set as 300 nm, which is a characteristic height for the dielectric structural colors. The higher nanostructures may lead to better performance, but the nanostructures are easy to collapse. Therefore, the thicknesses of the TiO_2 is set as 140 nm (see the details in Figure S3). Moreover, the excitation
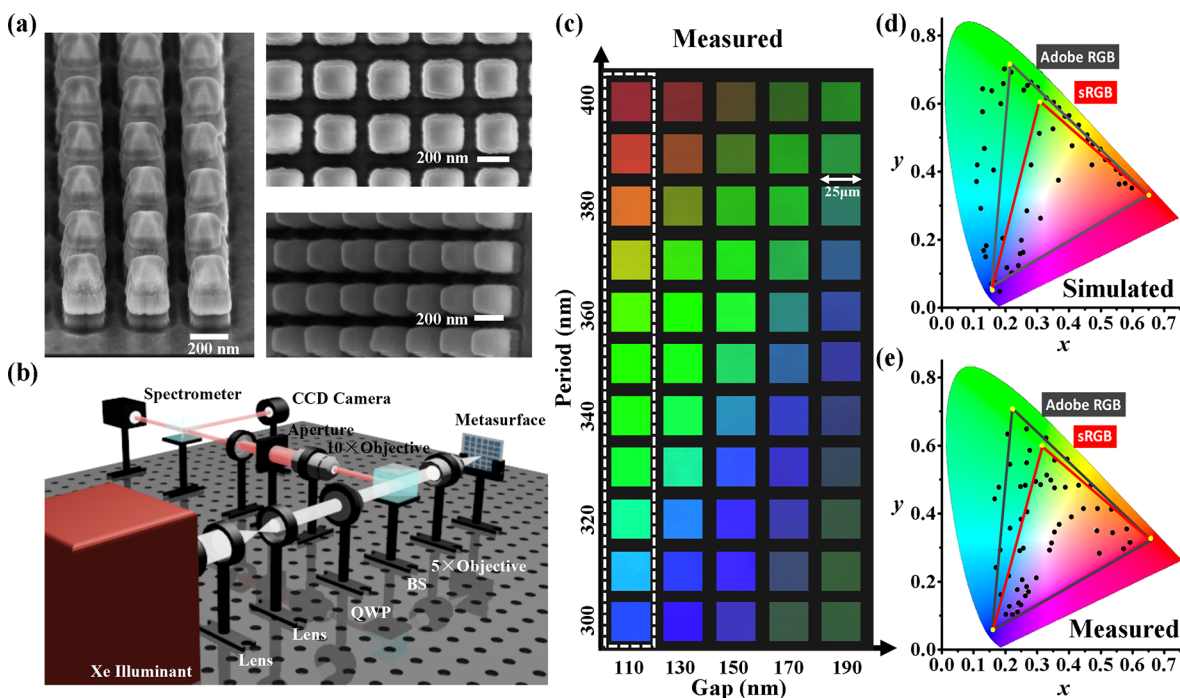
Figure 3. Experimental setup and color gamut of multi-dielectric metasurface. (a) SEM images of the multi-dielectric nanostructures. The scale bar is 200 nm. (b) Schematic illustrating the home-built setup to measure spectra by spectrometer and capture color images by CCD camera. The 5× and 10× objectives were used to make light incident on the sample normally and magnify reflected light, respectively. (c) Color palette captured by CCD camera with varying period and gap. Each sample is 25 μm × 25 μm. (d, e) The corresponding CIE 1931 chromaticity coordinates based on (d) simulated spectra and (e) measured spectra for the 55 samples in the color palette. Both of the color spaces of the measurement and the simulation exceed the Adobe RGB space.

of EQ at visible wavelength can be tuned by changing the refractive index of the capping layer (see the details in Figure S4). We also simulated the intensity of the multipolar decomposition for different refractive indices of Si_3N_4 layer (see the details in Figure S5). The index matching condition is not strictly fulfilled with varying the refractive indices, leading to locally modulating the intensity of different multipolar modes. The insets of Figure 2e,f show the details of multipolar decomposition ranging from 400 to 500 nm for two kinds of nanostructures. It is clear to see that the multipolar modes can be dramatically suppressed at short wavelengths in the multi-dielectric nanostructures.

Because the monochromaticity of spectra is drastically enhanced by the deep-modulated nanostructures, we can demonstrate that more than 85% energy of the whole reflection spectra can be confined in reflected peaks. According to the CIE XYZ tris-timulus values equation:

$$X = \frac{1}{k} \int D(\lambda) R(\lambda) \bar{x}(\lambda) d\lambda$$

$$Y = \frac{1}{k} \int D(\lambda) R(\lambda) \bar{y}(\lambda) d\lambda,$$

$$Z = \frac{1}{k} \int D(\lambda) R(\lambda) \bar{z}(\lambda) d\lambda \tag{2}$$

where $R(\lambda)$ represents reflection spectra, and $D(\lambda)$ is the energy distribution of the illumination. The spectra with higher monochromaticity can generate purer colors that are further from the white point in the center (0% saturation) and closer to solid colors on the CIE-space outline (100% saturation). Hence, the implementation of multi-dielectric nanostructures can dramatically increase saturation and color gamut space. We

adopt a system of 11 units to compare the saturation and hue for multi-dielectric and all-TiO_2 nanostructures in panels g and h of Figure 2, respectively. The gap size for every unit is fixed at 150 nm when the period varies from 300 to 400 nm with a step size of 10 nm. Based on Grassmann's law,[43] the saturation and hue can be calculated from simulated reflection spectra. We use the hue system in Lch (lightness, chroma, and hue) mode, in which 0° (360°) is red, 90° is yellow, 180° is green, and 270° is blue. For both nanostructures, almost full hue can be covered from 40° to 300° along with varying periods. Compared with all-TiO_2 nanostructures, the saturation of multi-dielectric nanostructures is significantly enhanced, particularly for aquamarine blue and green (n = 3−5). All 11 units show very pure colors with high saturation of more than 70%; for instance, the saturation can even reach 90% when the period is set as 380 nm (n = 9). The corresponding CIE 1931 chromaticity coordinates shown in the insets more intuitively present full hue coverage and drastic saturation enhancement. The angle-dependence properties of the multi-dielectric and all-TiO_2 nanostructures for both s- and p-polarization states are also investigated in Figure S6. The highly saturated structural colors of the multi-dielectric nanostructures are nearly independent of incident angle for the s-polarization state, which is very important for display applications.

To experimentally demonstrate the design properties, we fabricated the multi-dielectric nanoblocks array by electron beam lithography and plasma etching. Figure 3a presents side-view and top-view scanning electron microscope (SEM) images of multi-dielectric nanoblocks arrayed on silica substrate. The color contrast in side-view SEM images clearly shows layer distributions consisting of an SiO_2 capping layer on the top, a TiO_2 spacer layer in the middle, and an Si_3N_4
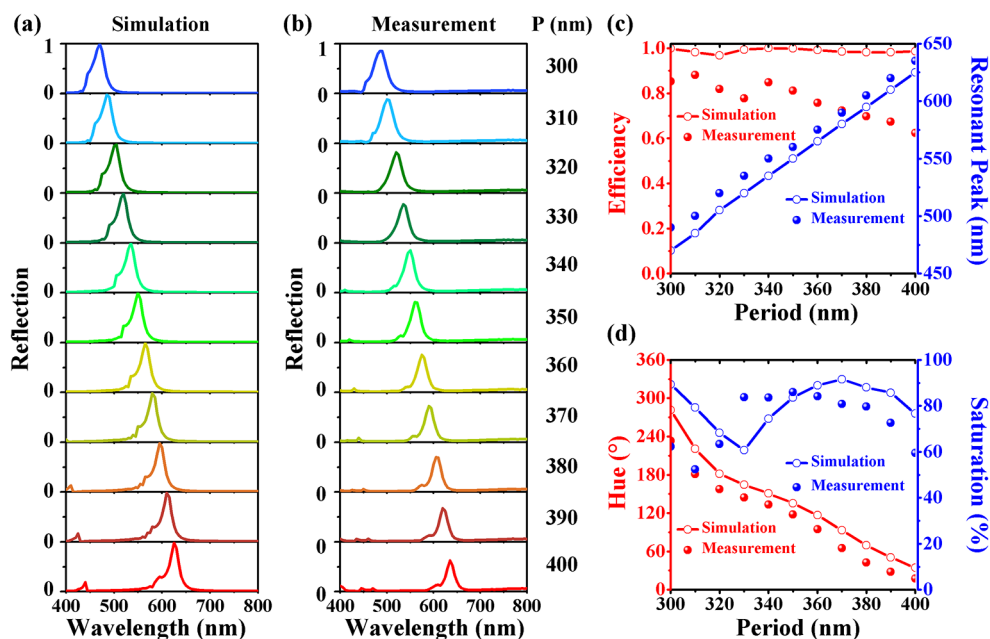
Figure 4. Simulated and measured results of pixels indicated by dashed boxes in Figure 3c. (a, b) Simulated and measured reflection spectra for multi-dielectric nanostructures with the increasing period ranging from 300 to 400 nm when the gap is fixed at 110 nm, respectively. (c, d) The comparison between measurement and simulations in (c) efficiency and resonant peak of reflection spectra and (d) hue and saturation of reflected colors. The solid line and scattered dots represent simulated and measured results, respectively.

layer at the bottom. The reflection measurement of the fabricated samples was performed by using the home-built optical setup illustrated in Figure 3b. We used a xenon lamp as light source to provide high-power and stable white light. The collimated linear polarized light was normally incident on the metasurface by a system of convex lens and a quarter polarizer. Due to the small sample area of 25 μm × 25 μm, 5× objective lens (numerical aperture, NA, of 0.13) and 10× objective lens (NA of 0.3) were, respectively, used in the incident path and reflected path of the setup. Taking advantage of the reversed 10× objective lens (NA of 0.3), the enlarged sample pattern can easily couple into charge-coupled device (CCD) camera for optical images and the spectrograph for the reflection spectra.

Figure 3c presents the measured optical images of 55 samples with different periods and gap size in reflection mode by CCD camera. As shown in the color palette, the hue of colors gradually varies from blue to red with increasing of period from 300 to 400 nm in 10 nm increments. Inversely, when the gap size increases from 110 to 190 nm with step size of 20 nm, the hue is blue-shifted, accompanying reduced saturation. That is because the high saturation for reflected waves is an optimized balance between the high reflected power and narrow reflected fwhm to minimize the gray color background, i.e., the small peaks and background that are away from the designed colors. We optimized the multi-dielectric nanostructures with gap size of 110 nm to obtain a high saturation. The saturation will be reduced for gap size away from the optimized one. A large gap size is utilized in the simulation to make sure that the unit cells do not interact with each other, which is a basic condition to independently control the color patterns pixel by pixel. However, increasing gap size can lead to a decrease in the effective refractive and scattering cross-section of the nanostructures, further resulting in blue-shifted spectra. Because the performances of colors strongly

hinge on the geometric size of the nanoblock, the hue and saturation of structural colors generated from multi-dielectric nanostructures can be flexibly adjusted by designing the period and the gap size. Furthermore, when the gap size is fixed at 110 nm, it is clear that nanostructures with arbitrary periods exhibit highly saturated colors, in accordance to the aforementioned mechanisms. We simulated and measured the CIE 1931 chromaticity coordinates of the 55 samples in panels d and e of Figure 3, respectively. It is noteworthy the simulated color gamut (Figure 3d) is quite wide, even taking up 57% CIE chromaticity space. There are many critical standard color spaces for display and imaging field in chromaticity diagram. Since 1996, the most significant standard spaces are summed up as (1) sRGB color space in 1996 used for monitors, printers, and the Internet; (2) Adobe RGB color space in 1999 used for advance imaging applications and high-end cameras; (3) DCI-P3 color space in 2005 used for digital movie projection; and (4) Rec. 2020 color space in 2012 used for ultrahigh-definition television (UHDTV). Nonetheless, there has been almost no existing content for realizing Rec. 2020 space yet. To confirm the color coverage of the proposed multi-dielectric nanostructures, we quantitatively compare the color gamut with the four standard spaces via calculating the area (see the details in Figure S7). As a result, we can conclude that the simulated color gamut occupies 171% sRGB, 127% Adobe, 126% DCI-P3, and 90% Rec. 2020; this clearly indicates the multi-dielectric nanostructures have great potentials for display applications. However, the measured color gamut represents the areal ratio of 128% for sRGB, 95% for Adobe RGB, 94% for DCI-P3, and 68% for Rec. 2020 in Figure 3e. Here, slightly variation could be attributed to the imperfection of the fabricated samples. Nevertheless, the measured color space in CIE diagram agrees reasonably well with the simulated one.
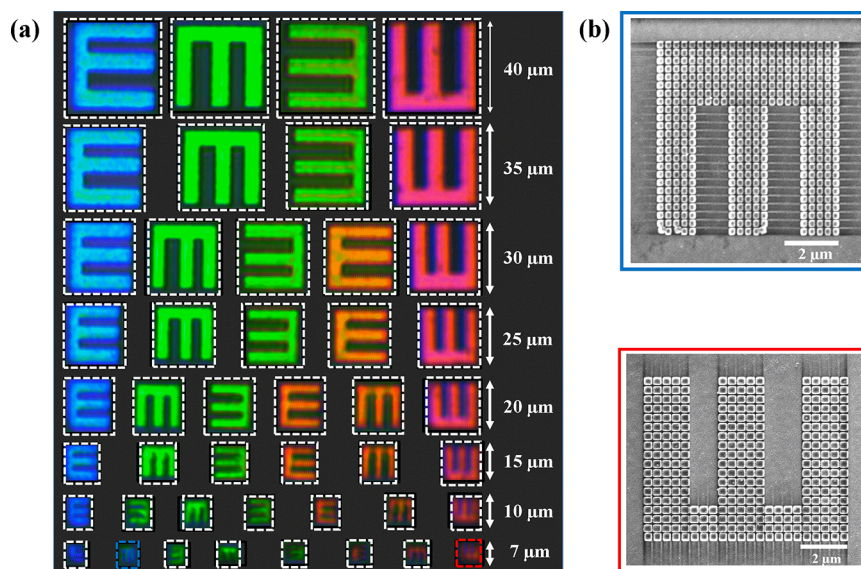
Figure 5. Colorful eye chart printed by multi-dielectric nanostructures. (a) The reflected images for fabricated "E" patterns with different sizes captured by CCD camera. A 10× objective (NA = 0.3) was used in the measurement. (b) Top-view SEM images for the 7 μm patterns with period of 310 nm (highlighted by blue box) and 400 nm (highlighted by red box), respectively. The scale bar is 2 μm.

To further investigate the performance of the structural colors in experiment, we quantitatively compare the measured and simulated spectra from spectrograph and COMSOL Multiphysics.[39] Figure 4a shows the simulated spectra of multi-dielectric nanostructures with periods varying from 300 to 400 nm when the gap is fixed at 110 nm. The actual cross-section of the fabricated sample has an 83° trapezoidal angle due to different etch resistances of multi-dielectric layers. To reduce the error between the simulated and experimental results, we adjusted the quadrate cross-section of the multi-dielectric nanostructures into trapezoidal cross-section with an 83° trapezoidal angle in simulated spectra, as shown in Figure 4a. The effective width of the nanostructures is decreased, and the gap size is consequently increased as existing trapezoidal cross-section for the fabricated sample. Therefore, there are some differences in the reflection spectra between the optimized and adjusted results of Figures 2d and 4a, respectively. As the period increases, there is a red shift for reflection peaks from 480 to 625 nm with almost 100% efficiency. The calculated spectra of all multi-dielectric nanostructures show high monochromaticity resulting from modulation of multipolar modes at visible wavelength. However, the reflection spectra have a blue shift with decreasing efficiency when the gap increases. This is because the reduced filling factor of multi-dielectric nanostructures leads to lower light-matter interaction (see the details in Figure S8). It is obvious that the simulated spectra are in good accord with the corresponding measured spectra shown in Figure 4b. When the period is fixed at 300 nm, for instance, the resonant peak is at 480 nm with 34 nm full width of half-maximum (fwhm) in simulation and at 490 nm with 32 nm fwhm in measurement, respectively. Figure 4c more intuitively depicts the resonant peak and efficiency of simulated and measured spectra. The slight shift of resonant peak results from the minute structural deviation from fabricated tolerances. Although the amplitude of measured spectra is lower compared to almost 100% efficiency in simulation, the measured efficiency still ranges from 88.1% to 62.3% when the period changes from 300 to 400 nm. The slightly lower

efficiency for measured results is mainly induced by imperfect sample fabrication. Although the reflection efficiency slightly decreases with increasing of the period, the measured reflection spectra are in satisfying agreement with simulated results. We further compare the measured and simulated colors by calculating saturation and hue in Figure 4d. Highly saturated measured colors with full hue are obtained, which is in good agreement with the simulated results.

To demonstrate the resolution of the highly saturated colors, we design a "colorful eye chart" in Figure 5. The "E" patterns in each row are composed of multi-dielectric nanostructures with varying periods at fixed gap size. The pattern sizes in different rows gradually decrease from 40 to 7 μm. Figure 5a shows the reflection images of the eye chart captured by CCD camera through a 10× objective (NA of 0.3). Clearly, three primary colors with high saturation are obtained in the printing pictures. Structural colors can distinctly vary from blue to red with varying periods. In the last row, the colorful patterns are slightly blur owing to small NA of the objective. Figure 5b shows the enlarged SEM images for two 7 μm patterns with period of 310 nm in the blue box and 400 nm in the red box, respectively. It is clear that the patterns are displayed by utilizing approximately 1.4 μm × 1.4 μm pixels. Hence, the sub-wavelength resolution for the multi-dielectric nanostructures can at least reach 18 000 dpi, which is high enough for display and imaging applications. In addition, the structural colors are very stable regardless of the size of the patterns, especially the green. For instance, 4 pixels × 4 pixels with unit cells arranged in a 350 nm period can still display highly saturated green.

In conclusion, we theoretically and experimentally demonstrated ultrahigh-saturation colors capitalizing multi-dielectric nanostructures on silica substrate. Compared with monodielectric nanostructures, the multi-dielectric design can realize deep modulation for Mie resonance. The suppression of multipolar modes at short wavelengths via the index matching of the SiO_2 capping layer between the TiO_2 layer and air and the Si_3N_4 bottom layer between silica substrate and TiO_2 layer can dramatically enhance the monochromaticity of reflection

spectra or, in other words, the saturation of visible colors. Wide color gamut occupying 127% in theory and 95% in measurement of Adobe RGB space can be realized by tuning the gap and period of nanostructures. Furthermore, the color space generated from multi-dielectric nanostructures can also cover most of standard color spaces in chromatic diagram; in particular, Rec. 2020, which is an important new standard, can be taken up 90% in theory. We believe that the multi-dielectric design for ultrahighly saturated colors is promising to form a new paradigm for advanced display applications, such as advance imaging, digital movie projection, ultrahigh-definition television (UHDTV), high-end camera, high-density optical data storage, and so on. Moreover, the proposed anti-reflection coating design is a general platform and can be used to further improve saturation of other structural color designs such as Si nanostructures.

Methods. The proposed multi-dielectric nanoblocks array was fabricated by electron-beam lithography and plasma etching. First, Si_3N_4, TiO_2, and SiO_2 were deposited on silica substrate successively in a plasma-enhanced chemical vapor deposition system (PECVD) from Plasmalab 100 (Oxford), an AJA magnetron sputtering system, and the PECVD again. A square array was printed by electron-beam lithography (Raith150) after a positive electron-beam resist (ZEP520A from Zeon Chemicals) was coated on the materials layer. A 30 nm thick Al as etch mask was deposited by e-beam evaporation (Temescal BJD-2000), accompanied by a lift-off process in which the sample is soaked in a resist remover (ZDMAC from ZEON Co.). Using CHF3 gas, three-layer nanoblocks were etched in inductively coupled plasma-reactive ion etching (Plasmalab System 100, Oxford). Finally, the residual Al was removed by Al wet etchant (a mixture of H_3PO_4, HNO_3, acetic acid, and water).

ASSOCIATED CONTENT

⑤ Supporting Information

The Supporting Information is available free of charge on the ACS Publications website at DOI: 10.1021/acs.nano-lett.8b04923.

Additional details on multipolar mode analysis, multi-polar-decomposition equations, a comparison among different anti-reflection designs, the role of SiO_2 capping layer and Si_3N_4 bottom layer, index matching and modulated impact for various capping layer and bottom layer, angle-dependence properties, a comparison among areas of distinct gamut, and the influence of gap size (PDF)

AUTHOR INFORMATION

Corresponding Authors

*E-mail: duk.choi@anu.edu.au.

*E-mail: schen@nankai.edu.cn.

ORCID ⓘ

Shuqi Chen: 0000-0002-7898-4148

Author Contributions

S.C. initiated and supervised the project. B.Y. and W. L. performed the numerical simulations and experiments. B.Y., W.L., Z.L., H.C., D.-Y.C., S.C., and J.T. prepared the manuscript. All the authors contributed to the analyses and discussions of the manuscript.

REFERENCES

(1) Kinoshita, S.; Yoshioka, S.; Miyazaki, J. *Rep. Prog. Phys.* **2008**, *71*, 074601.

(2) Xu, T.; Shi, H.; Wu, Y.-K.; Kaplan, A. F.; Ok, J. G.; Guo, L. J. *Small* **2011**, *7*, 3128−3136.

(3) Gu, Y.; Zhang, L.; Yang, J. K.; Yeo, S. P.; Qiu, C.-W. *Nanoscale* **2015**, *7*, 6409−6419.

(4) Shrestha, V. R.; Lee, S.-S.; Kim, E.-S.; Choi, D.-Y. *Nano Lett.* **2014**, *14*, 6672−6678.

(5) Clausen, J. S.; Hojlund-Nielsen, E.; Christiansen, A. B.; Yazdi, S.; Grajower, M.; Taha, H.; Levy, U.; Kristensen, A.; Mortensen, N. A. *Nano Lett.* **2014**, *14*, 4499−4504.

(6) Goh, X. M.; Zheng, Y.; Tan, S. J.; Zhang, L.; Kumar, K.; Qiu, C.-W.; Yang, J. K. *Nat. Commun.* **2014**, *5*, 5361.

(7) Goh, X. M.; Ng, R. J.; Wang, S.; Tan, S. J.; Yang, J. K. *ACS Photonics* **2016**, *3*, 1000−1009.

(8) Cheng, F.; Gao, J.; Luk, T. S.; Yang, X. *Sci. Rep.* **2015**, *5*, 11045.

(9) King, N. S.; Liu, L.; Yang, X.; Cerjan, B.; Everitt, H. O.; Nordlander, P.; Halas, N. J. *ACS Nano* **2015**, *9*, 10628−10636.

(10) Li, Z.; Clark, A. W.; Cooper, J. M. *ACS Nano* **2016**, *10*, 492−498.

(11) Tan, S. J.; Zhang, L.; Zhu, D.; Goh, X. M.; Wang, Y. M.; Kumar, K.; Qiu, C.-W.; Yang, J. K. *Nano Lett.* **2014**, *14*, 4023−4029.

(12) Proust, J.; Bedu, F.; Gallas, B.; Ozerov, I.; Bonod, N. *ACS Nano* **2016**, *10*, 7761−7767.

(13) Wood, T.; Naffouti, M.; Berthelot, J.; David, T.; Claude, J.-B.; Metayer, L.; Delobbe, A.; Favre, L.; Ronda, A.; Berbezier, I.; Bonod, N.; Abbarchi, M. *ACS Photonics* **2017**, *4*, 873−883.

(14) Vashistha, V.; Vaidya, G.; Hegde, R. S.; Serebryannikov, A. E.; Bonod, N.; Krawczyk, M. *ACS Photonics* **2017**, *4*, 1076−1082.

(15) Flauraud, V.; Reyes, M.; Paniagua-Dominguez, R.; Kuznetsov, A. I.; Brugger, J. *ACS Photonics* **2017**, *4*, 1913−1919.

(16) Nagasaki, Y.; Suzuki, M.; Takahara, J. *Nano Lett.* **2017**, *17*, 7500−7506.

(17) Wu, C.; Arju, N.; Kelp, G.; Fan, J. A.; Dominguez, J.; Gonzales, E.; Tutuc, E.; Brener, I.; Shvets, G. *Nat. Commun.* **2014**, *5*, 3892.

(18) Schuller, J. A.; Zia, R.; Taubner, T.; Brongersma, M. L. *Phys. Rev. Lett.* **2007**, *99*, 107401.

(19) Miyata, M.; Hatada, H.; Takahara, J. *Nano Lett.* **2016**, *16*, 3166−3172.

(20) Zhu, X.; Vannahme, C.; Hojlund-Nielsen, E.; Mortensen, N. A.; Kristensen, A. *Nat. Nanotechnol.* **2016**, *11*, 325.

(21) Song, M.; Li, X.; Pu, M.; Guo, Y.; Liu, K.; Yu, H.; Ma, X.; Luo, X. *Nanophotonics* **2018**, *7*, 323−331.

(22) Zhu, X.; Yan, W.; Levy, U.; Mortensen, N. A.; Kristensen, A. *Science Advances* **2017**, *3*, No. e1602487.

(23) Wang, H.; Wang, X.; Yan, C.; Zhao, H.; Zhang, J.; Santschi, C.; Martin, O. J. *ACS Nano* **2017**, *11*, 4419−4427.

(24) Kumar, K.; Duan, H.; Hegde, R. S.; Koh, S. C.; Wei, J. N.; Yang, J. K. *Nat. Nanotechnol.* **2012**, *7*, 557−561.

(25) Dong, Z.; Ho, J.; Yu, Y. F.; Fu, Y. H.; Paniagua-Dominguez, R.; Wang, S.; Kuznetsov, A. I.; Yang, J. K. *Nano Lett.* **2017**, *17*, 7620−7628.

(26) Masaoka, K. *IEEE access* **2016**, *4*, 3878−3886.

(27) Masaoka, K.; Nishida, Y.; Sugawara, M.; Nakasu, E. *IEEE Trans. Broadcast.* **2010**, *56*, 452−457.

(28) Groever, B.; Chen, W. T.; Capasso, F. *Nano Lett.* **2017**, *17*, 4902−4907.

(29) Khorasaninejad, M.; Zhu, A. Y.; Roques-Carmes, C.; Chen, W. T.; Oh, J.; Mishra, I.; Devlin, R. C.; Capasso, F. *Nano Lett.* **2016**, *16*, 7229−7234.

(30) Fan, Q.; Wang, D.; Huo, P.; Zhang, Z.; Liang, Y.; Xu, T. *Opt. Express* **2017**, *25*, 9285−9294.

(31) Mueller, J. P. B.; Rubin, N. A.; Devlin, R. C.; Groever, B.; Capasso, F. *Phys. Rev. Lett.* **2017**, *118*, 113901.

(32) Sun, S.; Zhou, Z.; Zhang, C.; Gao, Y.; Duan, Z.; Xiao, S.; Song, Q. *ACS Nano* **2017**, *11*, 4445−4452.

(33) Yang, B.; Liu, W.; Li, Z.; Cheng, H.; Chen, S.; Tian, J. *Adv. Opt. Mater.* **2018**, *6*, 1701009.

(34) Ma, Z.; Hanham, S. M.; Albella, P.; Ng, B.; Lu, H. T.; Gong, Y.; Maier, S. A.; Hong, M. *ACS Photonics* **2016**, *3*, 1010−1018.

(35) Liu, S.-D.; Leong, E. S.; Li, G.-C.; Hou, Y.; Deng, J.; Teng, J. H.; Ong, H. C.; Lei, D. Y. *ACS Nano* **2016**, *10*, 1442−1453.

(36) Zhang, Y.; Liu, W.; Li, Z.; Li, Z.; Cheng, H.; Chen, S.; Tian, J. *Opt. Lett.* **2018**, *43*, 1842−1845.

(37) Smirnova, D.; Kivshar, Y. S. *Optica* **2016**, *3*, 1241−1255.

(38) Yang, D.-J.; Im, S.-J.; Pan, G.-M.; Ding, S.-J.; Yang, Z.-J.; Hao, Z.-H.; Zhou, L.; Wang, Q.-Q. *Nanoscale* **2017**, *9*, 6068−6075.

(39) COMSOL. *Multiphysics*, Version *5.0*; COMSOL, Inc: Burlington, MA, 2016.

(40) Kaelberer, T.; Fedotov, V. A.; Papasimakis, N.; Tsai, D. P.; Zheludev, N. I. *Science* **2010**, *330*, 1510−1512.

(41) Campione, S.; Basilio, L. I.; Warne, L. K.; Sinclair, M. B. *Opt. Express* **2015**, *23*, 2293−2307.

(42) Zu, S.; Bao, Y.; Fang, Z. *Nanoscale* **2016**, *8*, 3900−3905.

(43) Fairman, H. S.; Brill, M. H.; Hemmendinger, H. *Color Res. Appl.* **1997**, *22*, 11−23.